

BCDDM: Branch-Corrected Denoising Diffusion Model for Black Hole Image Generation

AO LIU,^{1,*} ZELIN ZHANG,^{2,*} SONGBAI CHEN,^{2,3,†} CUIHONG WEN,^{1,‡} AND JIECI WANG^{2,§}

¹College of information science and engineering, Hunan Normal University, Changsha, 410081, People's Republic of China

²Department of Physics, Institute of Interdisciplinary Studies, Key Laboratory of Low Dimensional Quantum Structures and Quantum Control of Ministry of Education, Synergetic Innovation Center for Quantum Effects and Applications, Hunan Normal University, Changsha, Hunan 410081, People's Republic of China

³Center for Gravitation and Cosmology, College of Physical Science and Technology, Yangzhou University, Yangzhou 225009, People's Republic of China

ABSTRACT

The properties of black holes and accretion flows can be inferred by fitting Event Horizon Telescope (EHT) data to simulated images generated through general relativistic ray tracing (GRRT). However, due to the computationally intensive nature of GRRT, the efficiency of generating specific radiation flux images needs to be improved. This paper introduces the Branch Correction Denoising Diffusion Model (BCDDM), which uses a branch correction mechanism and a weighted mixed loss function to improve the accuracy of generated black hole images based on seven physical parameters of the radiatively inefficient accretion flow (RIAF) model. Our experiments show a strong correlation between the generated images and their physical parameters. By enhancing the GRRT dataset with BCDDM-generated images and using ResNet50 for parameter regression, we achieve significant improvements in parameter prediction performance. This approach reduces computational costs and provides a faster, more efficient method for dataset expansion, parameter estimation, and model fitting.

1. INTRODUCTION

The recent release of black hole images by the Event Horizon Telescope (EHT) collaboration provides direct evidence for the existence of black holes in the universe (Event Horizon Telescope Collaboration et al. 2019a, 2022a, 2024a). These observations offer a unique opportunity to probe the electromagnetic interactions, material distribution, and accretion processes near black holes, further testing the validity of gravity theories and accretion disk models (Mizuno et al. 2018; Event Horizon Telescope Collaboration et al. 2021a,b; Narayan et al. 2021; Event Horizon Telescope Collaboration et al. 2024b,c, 2022b,c; Liu et al. 2022; Wang et al. 2022; Zhang et al. 2022; Qin et al. 2022; Chen et al. 2023; Zhang et al. 2024; Zhang et al. 2024; Hou et al. 2024). Accretion disks, as the primary sources of visible light around black holes, significantly influence the resulting images. For the current EHT targets, M87* and Sgr A*, the surrounding hot plasma is considered to be part of a radiatively inefficient accretion flow (RIAF) (Igumenshchev et al. 2003; Narayan et al. 2003; Yuan &

* These authors contributed equally to this work.

† Corresponding author: csb3752@hunnu.edu.cn

‡ Corresponding author: cuihongwen@hunnu.edu.cn

§ Corresponding author: jieciwang@hunnu.edu.cn

31 Narayan 2014; Event Horizon Telescope Collaboration et al. 2019b, 2022c; Narayan et al. 2022). Such flows
32 are typically hot, geometrically thick, and optically thin at an observing frequency of 230 GHz, making it
33 possible to observe features close to the event horizon, such as the photon ring, black hole shadow and inner
34 shadow (Bardeen 1973; Falcke et al. 2000; Gralla et al. 2019; Johnson et al. 2020; Chael et al. 2021; Peng et al.
35 2021). At an observational frequency of 230 GHz, the emission we primarily detected comes from synchrotron
36 radiation produced by relativistic electrons. However, in the strong gravitational field near black holes, it is
37 not possible to directly infer information about the plasma density, temperature, velocity, or magnetization
38 of accretion disks from the observed images alone. This is typically achieved through general relativistic
39 ray tracing (GRRT) (Luminet 1979; Vincent et al. 2011; Pu et al. 2016b; Gelles et al. 2021; White 2022;
40 Huang et al. 2024). By fitting observational data from the EHT to simulated images produced by GRRT,
41 one can effectively extract information about the black hole and the surrounding accretion flow (Broderick
42 et al. 2020; Event Horizon Telescope Collaboration et al. 2021b, 2024b; Yfantis et al. 2024). GRRT involves
43 calculating simulated images of the black hole as seen by the observer, starting with backward ray tracing
44 from the observer to the black hole, followed by radiation transfer calculations through the radiative regions
45 of the accretion disk. However, due to the computationally intensive nature of this process, substantial
46 computational resources are often required. On one hand, to cover a large parameter space, simulations often
47 require the generation of millions of images, demanding significant computational power. On the other hand,
48 Bayesian parameter estimation of the model requires rapid generation of images corresponding to different
49 parameter sets, placing high demands on computational speed (Yfantis et al. 2024; Chang et al. 2024). Most
50 implementations have incorporated GPU acceleration or adaptive ray-tracing methods, yielding significant
51 improvements in computational efficiency (Chan et al. 2018; Gelles et al. 2021; Moscibrodzka & Yfantis 2023).
52 Recently, advancements in deep neural networks have enabled the generation of black hole images through
53 deep learning, providing a promising new approach for efficiently obtaining such images.

54 Deep learning models possess powerful feature learning and pattern recognition capabilities, enabling them
55 to extract valuable information from limited data (Krizhevsky et al. 2012; Hochreiter & Schmidhuber 1997;
56 Simonyan & Zisserman 2014). Recent applications of deep learning have shown notable effectiveness in black
57 hole parameter identification (van der Gucht et al. 2020; Qiu et al. 2023) and image reconstruction tasks
58 (Medeiros et al. 2018, 2023). Several highly effective models have been developed for image generation tasks,
59 offering robust methods for synthesizing realistic, high-quality images. Generative Adversarial Networks
60 (GANs), which are based on game theory (Goodfellow et al. 2014), use adversarial training to enable two

neural networks, namely the generator and the discriminator, to compete with each other, thereby enhancing the generator’s ability to produce high-quality samples. While GANs can generate highly realistic images through this adversarial process, the training can be unstable and is prone to mode collapse. Variational Autoencoders (VAEs) are another class of generative models that learn the probability distribution of data and can generate new samples similar to the training data (Kingma & Welling 2022). Compared to GANs, VAEs training is more stable; however, VAEs typically produce less realistic images, especially in terms of fine details. The generation of black hole images had been successfully achieved using both GANs (Mohan et al. 2024) and VAEs (SaraerToosi & Broderick 2024). Compared with GANs and VAEs, diffusion models have a wider range of practical applications (Ho et al. 2020). Due to the direct optimization of the logarithmic likelihood of the generation process during training, the diffusion model avoids the common mode collapse problem in GANs. The diffusion model gradually recovers the original data from Gaussian noise through a multi-step denoising process, and the generated samples have very high quality, especially in image generation tasks. The generated images have rich details and high resolution, avoiding the blurring problem of VAEs generated images.

Therefore, we propose a novel black hole image generation method, Branch-Corrected Denoising Diffusion Model (BCDDM), designed to rapidly produce high-quality black hole data. Diffusion models, as advanced image generation models, have demonstrated their capability to generate high-fidelity images across various domains (Asgar et al. 2023; Shi et al. 2024; Zheng et al. 2025; Tu et al. 2024; Ran et al. 2024). However, to the best of our knowledge, no prior research has applied them to black hole image generation. This study aims to explore whether BCDDM can learn the mapping between black hole parameters and images during the generation process. In conventional machine learning tasks involving images, data augmentation techniques such as random rotation and cropping are commonly employed. However, for black hole images, the size and orientation often carry specific physical significance, rendering such operations unsuitable as they may distort the interpretability of the data. BCDDM addresses this limitation by providing an alternative augmentation strategy—generating physically plausible synthetic images conditioned on parameter inputs, thereby expanding the training dataset while preserving physical consistency. To validate the utility of BCDDM-generated images, we train a ResNet50 regressor on both the original dataset and the augmented dataset produced by our model, aiming to demonstrate improved predictive performance for black hole parameters.

The main contributions of this article are as follows: Firstly, this paper presents an innovative diffusion architecture model, BCDDM, which addresses the limitations of traditional methods in accurately mapping

91 images to physical parameters during black hole image generation. By incorporating parameter correction
 92 branches and a mixed loss function, BCDDM significantly enhances the precision and diversity of the gener-
 93 ated images. Additionally, BCDDM is the first to apply diffusion algorithms to black hole image generation.
 94 The experimental results demonstrate that the model is capable of producing high-quality black hole images
 95 with a strong correlation to physical parameters, thereby offering novel tools and methodologies for astronom-
 96 ical observations and theoretical studies. Finally, the integration of a ResNet50-based black hole parameter
 97 regressor confirms the high fidelity of images produced by BCDDM and underscores the model’s substantial
 98 contribution to improving the performance of data-driven regressors in parameter prediction.

99 2. METHODOLOGY

100 2.1. Black hole image dataset

101 We generate a dataset using the radiatively inefficient accretion flow (RIAF) model (Narayan et al. 1997;
 102 Yuan & Narayan 2014), focusing exclusively on thermal synchrotron emission from the accretion flow. In such
 103 an accretion flow, the magnitude and distribution of the electron temperature and electron density directly
 104 affect the distribution and intensity of the radiation in the black hole image. The spatial distributions of the
 105 electron temperature \mathcal{T}_e and thermal electron density \mathcal{N}_e are described by

$$106 \quad \mathcal{N}_e = n_e r^{-\alpha} e^{-\beta}, \quad \mathcal{T}_e = T_e r^{-\gamma}, \quad \beta = \frac{z^2}{2\sigma^2}, \quad (1)$$

107 where $z \equiv r \cos \theta$, and the radial dependencies $\alpha = 1.1$ and $\gamma = 0.84$ are adopted from vertically averaged
 108 density and temperature profiles (Yuan et al. 2003; Pu et al. 2016a; Pu & Broderick 2018). The electron
 109 number density n_e and temperature T_e define the normalization of the electron distribution. The parameter
 110 σ controls the vertical thickness of the accretion flow, parameterized as $h_{\text{disk}} \equiv \sigma/x$, where $x \equiv r \sin \theta$.
 111 The geometry of the flow is thus determined by h_{disk} . The magnetic field strength B is assumed to be in
 112 approximate equipartition with the ions

$$113 \quad \frac{B^2}{8\pi} = \epsilon n_e \frac{m_p c^2 r_g}{6r}, \quad (2)$$

114 where $r_g = GM_{\text{BH}}/c^2$, m_p is the proton mass, and $\epsilon = 0.1$ (Broderick et al. 2011a,b, 2016; Pu et al. 2016a;
 115 Pu & Broderick 2018). The Keplerian factor k describes the degree to which the flow deviates from Keplerian
 116 motion ($k = 1$) or approaches free-fall ($k = 0$) (Pu et al. 2016a). A key limitation of the RIAF model is
 117 the lack of jet emission. For M87*, EHT observations at 230 GHz show significant synchrotron contributions
 118 from both the disk and the jet on horizon scales (Event Horizon Telescope Collaboration et al. 2019a,b). This
 119 omission in the model could be addressed in the future by employing more comprehensive models, such as

120 GRMHD simulations. We generate the dataset using the GRRT code *ipole* (Mościbrodzka & Gammie 2018),
 121 which calculates the radiation intensity distribution for simulated observational images. These images are
 122 produced at a frequency of 230 GHz, with a camera field of view of $160 \times 160 \mu\text{as}$ and resolution of 256×256 .
 123 To align with the M87* case, we fix the observer inclination angle at 163° and adjust the total flux density
 124 to 0.5 Jy (Event Horizon Telescope Collaboration et al. 2019b) by adjusting n_e . Seven physical parameters
 125 are varied in the simulation, with their respective value ranges provided in Table 1. The rotation direction
 126 of the accretion disk is randomly selected between -1 (clockwise) and 1 (counterclockwise), while the other
 127 six parameters are uniformly sampled within their respective ranges. Ultimately, we generate a set of 2157
 128 images for training BCDDM.

Table 1. Parameter ranges used in the RIAF black hole images generation.

Parameter	Symbol	Range
Black hole spin	a	$[-1, 1]$
Black hole mass	M_{BH}	$[5 \times 10^9 M_\odot, 8 \times 10^9 M_\odot]$
Electron temperature	T_e	$[10^{10} \text{ K}, 10^{12} \text{ K}]$
Accretion disk thickness	h_{disk}	$[0.1, 0.8]$
Keplerian factor	k	$[0, 1]$
Position angle	PA	$[0^\circ, 360^\circ]$
Fluid direction	F_{dir}	$-1, 1$

2.2. Data preprocessing

129 The parameters used for generating black hole images exhibit significant disparities in their orders of mag-
 130 nitude. As shown in Table 1, certain parameters like black hole spin and mass differ by up to 9 orders of
 131 magnitude. In deep learning frameworks, the inconsistency in magnitudes of data can lead to numerical com-
 132 putation problems such as gradient explosion or vanishing, which can seriously affect the training effectiveness
 133 and convergence performance of the model. To alleviate these numerical instabilities, we introduce Z-score
 134 normalization technique to preprocess black hole parameters (Fei et al. 2021). Z-score quantifies the standard
 135 deviation of a single data point relative to the mean of the entire dataset. Through Z-score, the raw data is
 136 transformed into a standard normal distribution, with its mean adjusted to 0 and standard deviation to 1,
 137 ensuring consistency in data scale. Let r denote the parameter category, where x_r represents the initial black
 138 hole parameter value, μ_r is the mean of the initial black hole parameters, and σ_r is their standard deviation.
 139 The normalized black hole parameter value z_r is given by the Z-score formula
 140

$$z_r = \frac{x_r - \mu_r}{\sigma_r}, \quad \text{for } r \in \{1, 2, \dots, 7\}. \quad (3)$$

142 where T_e was log-transformed prior to normalization. Z-score normalization is a reversible linear transforma-
 143 tion, allowing the original black hole parameters to be recovered from their normalized counterparts. To ensure
 144 training stability, we also apply Maximum Normalization to the black hole images. For each image, given the
 145 flux density $S(i, j)$ of each pixel, the normalized image S_{norm} is computed as $S_{\text{norm}}(i, j) = S(i, j)/S_{\text{max}}$, where
 146 $S_{\text{max}} = \max(S)$. This scales the pixel values to the range $[0, 1]$. Since all black hole images are adjusted to a
 147 total flux density of 0.5 Jy, the normalized images generated by the neural network can be rescaled back to
 148 their original physical dimensions by restoring the total flux density to 0.5 Jy.

149 2.3. Diffusion model framework

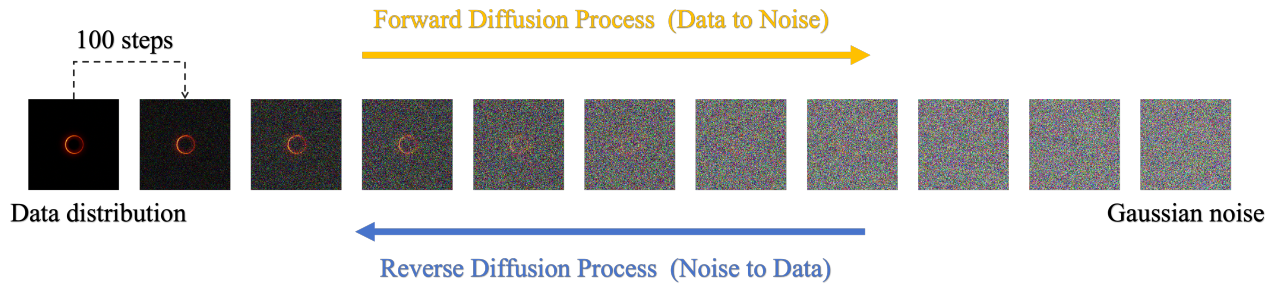


Figure 1. The diffusion process of black hole images. We output the image every 100 steps for a total of 1000 times to observe the changes in the diffusion process of the image.

150 The diffusion model initiates with a forward diffusion process applied to the black hole image, wherein Gaus-
 151 sian noise is incrementally introduced according to a predefined noise schedule. This process systematically
 152 corrupts the input image over T steps until it converges to a pure Gaussian noise distribution. The noise
 153 schedule, governed by the diffusion coefficients β_t , determines the magnitude of noise added at each step t .
 154 Specifically, the transition from x_{t-1} to x_t is formulated as

$$155 q(x_t|x_{t-1}) = \mathcal{N}(x_t; \sqrt{1 - \beta_t}x_{t-1}, \beta_t I), \quad (4)$$

156 which can equivalently be expressed as

$$157 x_t = \sqrt{1 - \beta_t}x_{t-1} + \sqrt{\beta_t}\epsilon_t, \quad (5)$$

158 where $\epsilon_t \sim \mathcal{N}(0, 1)$. The joint distribution of the entire forward process is given by

$$159 q(x_{1:T}|x_0) = \prod_{t=1}^T q(x_t|x_{t-1}). \quad (6)$$

160 As illustrated in Figure 1, the diffusion process is visualized for $T = 1000$ steps, with β_t initialized at 10^{-4} and
 161 linearly increasing to 0.02. The linear noise schedule ensures a smooth degradation of the black hole image
 162 into noise, balancing detail preservation in early stages with complete corruption in later stages.

163 During the training process, the model learns to reverse this process by predicting the noise introduced
 164 at each diffusion step. The denoising process involves estimating the conditional distribution $q(x_{t-1}|x_t, x_0)$,
 165 which is Gaussian with mean μ_t and variance β_t

$$166 \quad q(x_{t-1}|x_t, x_0) = \mathcal{N}(x_{t-1}; \mu_t, \beta_t I). \quad (7)$$

167 By defining $\alpha_t = 1 - \beta_t$ and $\bar{\alpha}_t = \prod_{s=1}^t \alpha_s$, the mean and variance can be derived as

$$168 \quad \mu_t = \frac{\alpha_t}{\sqrt{1 - \alpha_t}} \left(x_t - \frac{\sqrt{1 - \bar{\alpha}_t}}{\sqrt{1 - \alpha_t}} \epsilon_t \right) \quad (8)$$

$$169 \quad \beta_t = \frac{1 - \bar{\alpha}_{t-1}}{1 - \bar{\alpha}_t} \beta_t \quad (9)$$

171 This formulation enables the trained noise-prediction network to iteratively denoise random Gaussian noise,
 172 ultimately reconstructing a coherent black hole image from pure noise. The controlled and gradual nature
 173 of the diffusion process is critical for ensuring the model's ability to accurately reverse the noise addition,
 174 thereby facilitating high-quality sample generation.

175 2.4. Model architecture

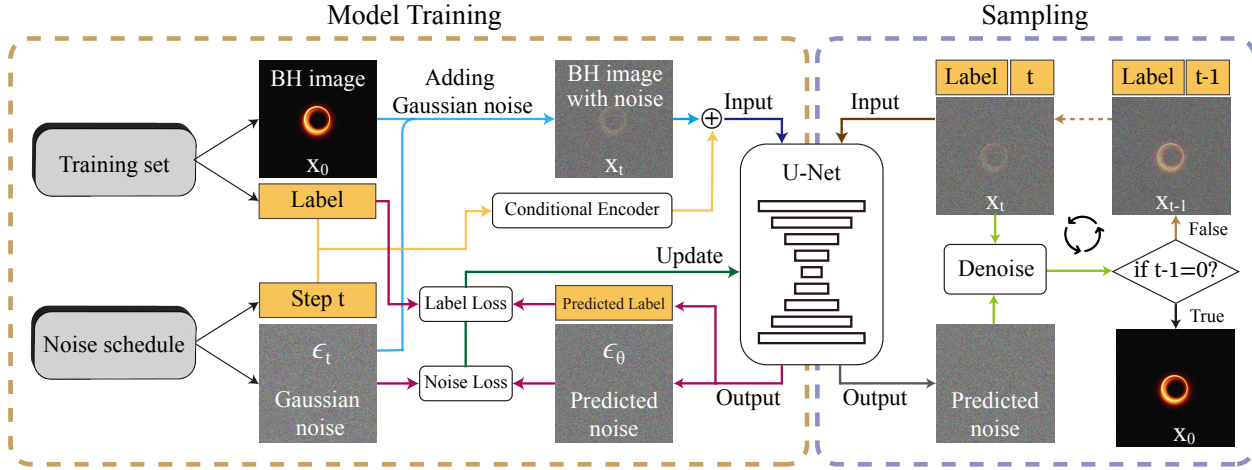


Figure 2. BCDDM architecture for black hole image generation. The diffusion process and denoising process utilize the same U-Net model, with detailed architecture illustrated in Figure 3.

176 The logical architecture of BCDDM for its training and sampling to generate images is shown in Figure 2.
 177 Our training set contains the black hole images we generated, and the seven physical parameters for generating
 178 the black hole images serve as the labels for each image. During training, the forward diffusion process is first
 179 applied to the original black hole image x_0 , progressively introducing noise according to the noise schedule.
 180 After t steps of noise addition, the resulting image x_t is obtained. To establish a correspondence between the
 181 black hole image and its physical parameters, we encode both the step t and the image's label, embedding

182 this information into the noisy image x_t . The core of our proposed model lies in a Branch-Corrected U-Net
 183 architecture designed to perform physically conditioned denoising, enabling the restoration of high-fidelity
 184 black hole images that align with the physical parameters. As shown in Figure 3, we enhance the standard
 185 U-Net architecture by introducing a parameter corrector branch at the lowest point of the downsampling
 186 path. This branch encodes the extracted features to learn the mapping between the image’s high-dimensional
 187 latent space distribution and the physical parameters. The Branch-Corrected U-Net simultaneously predicts
 188 both the noise component ϵ_θ and the parameter label. The model parameters are updated by minimizing the
 189 residuals between the predicted and actual noise, as well as between the predicted and ground truth labels,
 190 ensuring both denoising accuracy and physical fidelity.

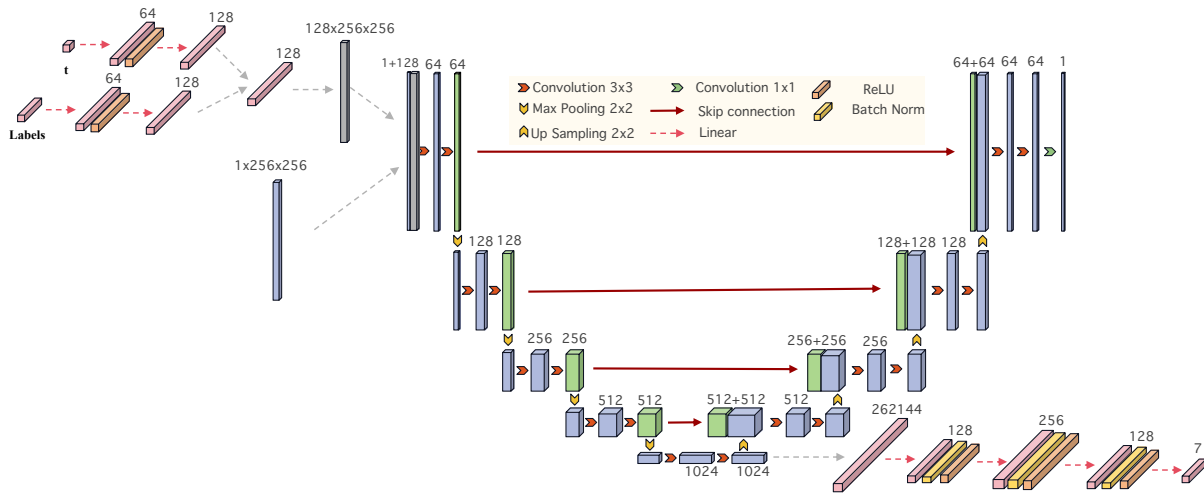


Figure 3. Encoding and Decoding architecture embedded in BCDDM. The trainable components consist solely of the input encoded label vector and black hole image, along with the output predicted parameters and noise.

191 To optimize the model, we design a composite loss function combining noise prediction loss L_{noise} and
 192 parameter consistency loss L_{label} (Wan & Ohtani 2000). The noise loss, defined as

$$193 \quad L_{\text{noise}} = \mathbf{E}_{t, x_0, \epsilon} \left[(\epsilon - \epsilon_\theta(x_t, t, l))^2 \right], \quad (10)$$

194 ensures high-quality image generation by penalizing deviations in noise estimation. Meanwhile, the label loss,

$$195 \quad L_{\text{label}} = \mathbf{E}_{x_0, l} \left[(f(k) - l)^2 \right], \quad (11)$$

196 where k denotes the feature vector extracted during downsampling and $f(k)$ its encoded representation,
 197 enforces alignment between generated images and their target physical parameters. The total loss is a weighted
 198 combination of these terms,

$$199 \quad L = \lambda_1 L_{\text{noise}} + \lambda_2 L_{\text{label}}, \quad (12)$$

where λ_1 and λ_2 balance the contributions of denoising and physical consistency during optimization. This dual-objective optimization ensures accurate denoising while preserving physical consistency.

Once the model training is completed, the reconstruction of a black hole image from input parameters can be achieved through a sampling process, as illustrated in Figure 2. The process begins by initializing the step $t = T$ and providing an initial Gaussian noise x_T along with the physical parameters of the black hole image as the label. These inputs are fed into the model, which predicts the noise component and subsequently denoises x_T to produce the image x_{T-1} at step $t = T - 1$. This iterative procedure is repeated, progressively reducing the noise at each step, until the final step $t = 0$ is reached. At this stage, the sampling process concludes, yielding the fully denoised black hole image x_0 conditioned on the physical parameter labels.

3. RESULTS

3.1. Generate Black Hole Image Results

The BCDDM model was trained on the RIAF black hole image dataset, which was partitioned into 1941 images for training and 216 images for validation. The noise schedule was configured with a total diffusion step $T = 1000$, where the diffusion coefficient β_t was initialized at 10^{-4} and linearly increased to 0.02. For optimization, we fixed the weighting coefficients in Eq. 12 as $\lambda_1 = 0.95$ and $\lambda_2 = 0.05$ throughout the training process. This configuration ensured the validation loss values of the noise and the label with a small difference, and they will ultimately be 5.27×10^{-4} and 4.13×10^{-4} , respectively. The learning rate was initially set to 3×10^{-3} and adjusted using a loss-driven decay strategy to improve model convergence. Specifically, after 500 epochs, if no improvement in validation loss was observed for 5 consecutive epochs, the learning rate was reduced by a factor of 0.97. This annealing process resulted in a final learning rate of approximately 1.07×10^{-5} , ensuring stable training dynamics while avoiding premature convergence to suboptimal solutions.

The model was trained for 8000 epochs, with the loss trajectory depicted in Figure 4. The initial phase exhibited a rapid decline in loss, followed by a slower convergence in later stages. Notably, the validation loss plateaued after 5000 epochs, while the training loss continued to decrease slowly, indicating the onset of overfitting. To illustrate the model’s performance progression, two independent black hole images were sampled at epochs 100, 1000, 2500, and 5000. The results demonstrate a clear correlation between decreasing loss and improving image clarity, with the generated images becoming progressively sharper as training advanced.

Using the model saved at the 5000th training epoch, we generate images from physical parameters and Gaussian noise. We select 6 images from an additional test dataset and reconstruct the corresponding black hole

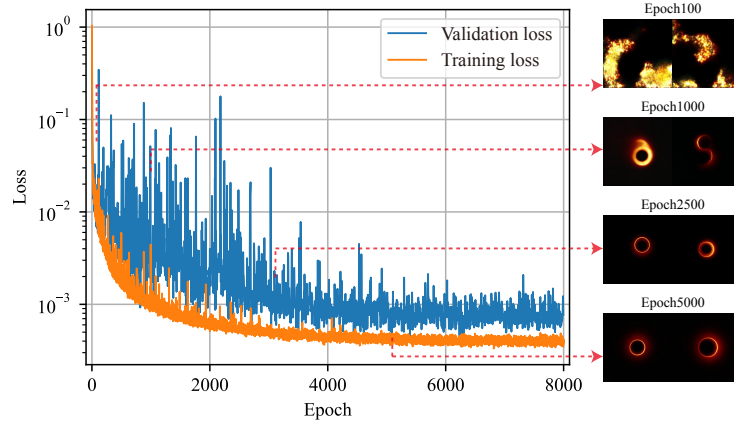


Figure 4. Training loss and validation loss during the training process. The right panel displays two independent black hole images generated by BCDDM at epochs 100, 1000, 2500, and 5000, illustrating the performance progression of the generative model.

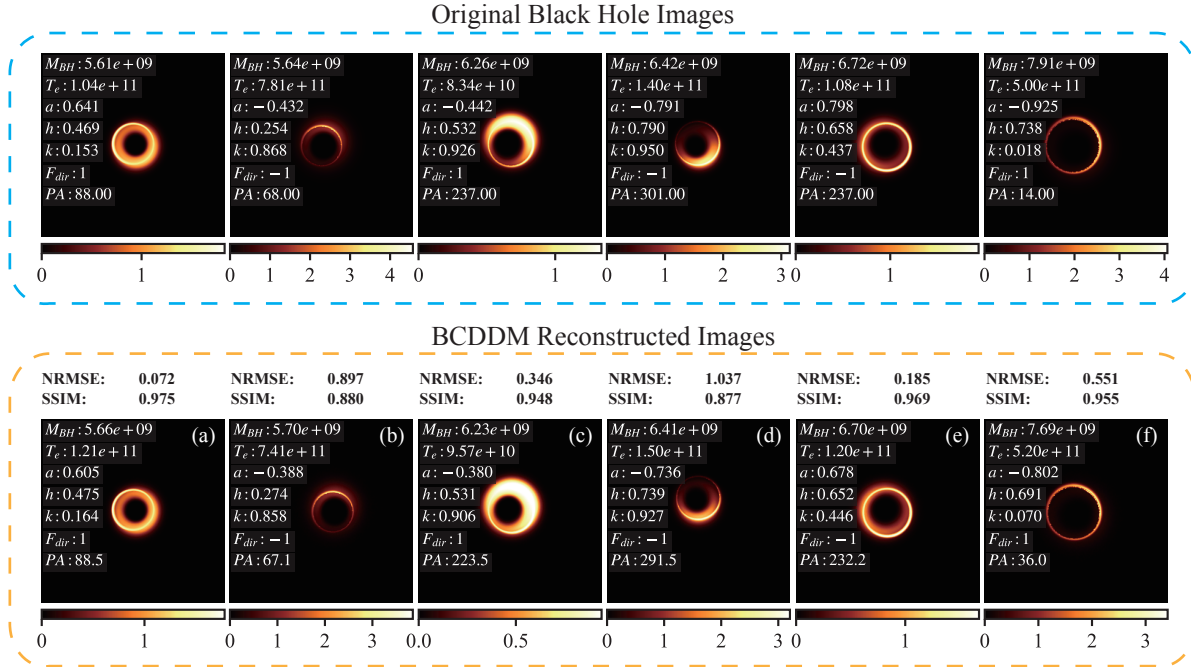


Figure 5. Comparison of original and reconstructed black hole images in the additional test set. The figure presents six pairs of GRRT-simulated original black hole images (top row) alongside their BCDDM-reconstructed counterparts (bottom row). The parameters displayed above the original images represent the ground truth values used as initial inputs, while those below the reconstructed images show the output from the parameter corrector branch. Each reconstructed image is annotated with its NRMSE (Normalized Root Mean Square Error) and SSIM (Structural Similarity index) values compared to the original. All images are rendered in brightness temperature units ($10^{10}K$), calculated as $T = S\lambda^2/(2k_B\Omega)$, where S denotes flux density, λ the observation wavelength, k_B the Boltzmann constant, and Ω the solid angle of the resolution element.

231 images using their associated parameter sets, as shown in Figure 5. In the original GRRT image, the initial
 232 parameters used for generating the image are overlaid for reference. Meanwhile, the BCDDM-reconstructed
 233 image displays the predicted output from the parameter correction branch. The results demonstrate that
 234 BCDDM produces images with consistent morphological and brightness distribution features compared to

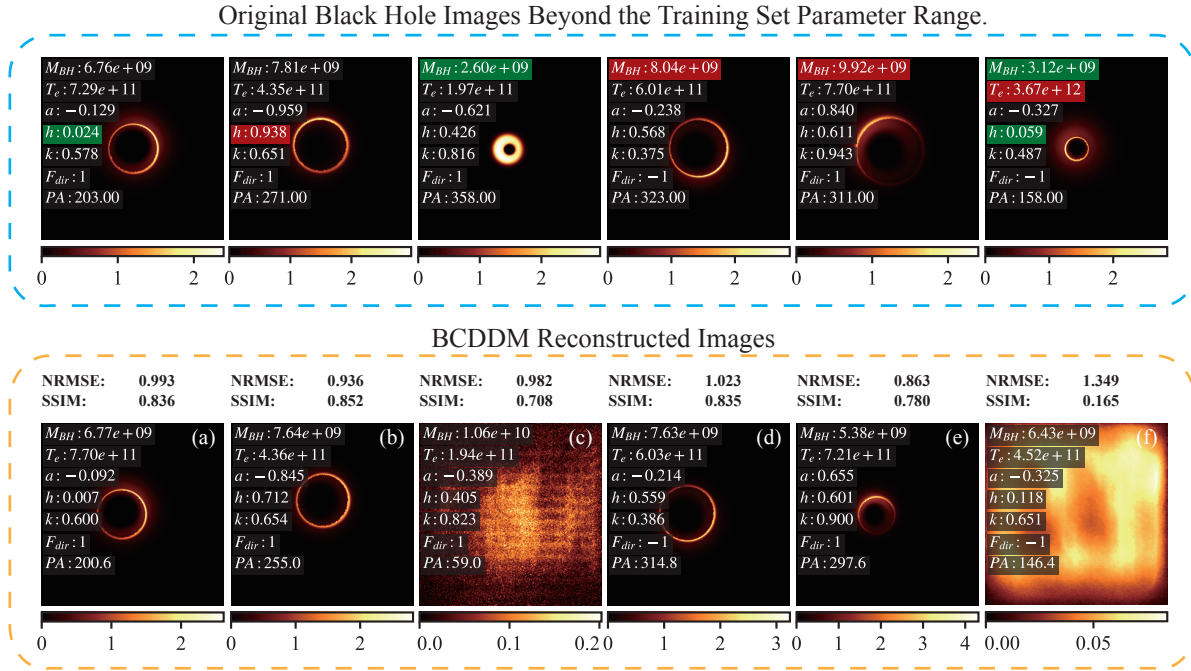


Figure 6. Comparison of the original and reconstructed black hole images, similar to Figure 5, but evaluated beyond the training dataset’s parameter range. Parameters marked in green indicate values below the original range, while those in red denote values above the range.

235 those generated by GRRT when using the same physical parameters. Key features such as the direct image
 236 of the accretion disk, photon ring, and inner shadow are accurately reconstructed. To quantify the similar-
 237 ity between the reconstructed and original images, we compute the Normalized Root Mean Squared Error
 238 (NRMSE) (Stephen & Kazemi 2014) and the Structural Similarity Index (SSIM) (Wang & Bovik 2009; Wang
 239 et al. 2004), displayed above each BCDDM-reconstructed image. NRMSE measures pixel-wise similarity, while
 240 SSIM emphasizes structural consistency, where an NRMSE of 0 and an SSIM of 1 indicate perfect agreement.
 241 Our analysis reveals high SSIM values across all reconstructed images. However, panels (b) and (d) in Figure
 242 5 exhibit relatively higher NRMSE values. This discrepancy arises because, despite the consistency in image
 243 features, the spatial alignment between BCDDM-generated and GRRT images occasionally varies, likely due
 244 to the influence of initial noise distribution during sampling from pure Gaussian noise. Additionally, differ-
 245 ences in the maximum values of the color bars indicate slight instability in the model’s brightness prediction,
 246 contributing to elevated NRMSE values, as seen in panels (c) and (f). The physical parameters predicted
 247 by the parameter correction branch closely match the original values, with only minor discrepancies observed
 248 in the spin parameter a and electron temperature T_e . This confirms that the parameter correction branch
 249 effectively learns the mapping between images and physical parameters, demonstrating BCDDM’s sensitivity
 250 to parameter variations.

Table 2. Dataset size and split for RLDs, FKDs, and MXDs.

Dataset	Train	Val	Test
RLDs	1725	216	216
FKDs	1725	216	216
MXDs	3450	216	216

While we selected an extensive parameter range for a , k , F_{dir} , and PA during training, the parameters M_{BH} , T_e , and h could potentially span even wider ranges. The model’s ability to reconstruct images beyond the original dataset’s parameter range provides insight into its generalization capabilities. Figure 6 presents six experiments where specific parameters were either increased or decreased beyond the original bounds. The results indicate that the model only achieves partial generalization for the accretion disk thickness h , successfully recovering the image structure as shown in panels (a) and (b). However, the model shows limited generalization for M_{BH} and T_e , while minor deviations from the training range yield consistent reconstructions (panel d), larger deviations result in either failed reconstructions (panels c and f) or artifacts in recovered features (panel e). All reconstructed images exhibit high NRMSE values, suggesting that the current model primarily specializes in the trained parameter space. Nevertheless, this limitation could be mitigated by expanding the parameter range of the training dataset.

3.2. Parameter Regression Evaluator

To evaluate the effectiveness of BCDDM in expanding the original RIAF black hole image dataset, we construct a deep learning-based black hole parameter regression model. This model is trained on both the original dataset and the dataset augmented by BCDDM. By comparing the model’s performance on these two datasets, we aim to determine whether the augmented dataset can enhance the prediction accuracy of the black hole parameter regression model.

The RIAF dataset serves as the foundation for constructing the real dataset (RLDs), which includes training, validation, and test sets. We then generate an equivalent number of black hole images using BCDDM through uniform random sampling within the parameter ranges specified in Table 1. Using a single RTX3090 graphics card, we can generate images at a speed of 5.25 seconds per image. The resulting datasets comprise three distinct configurations: the fake dataset (FKDs) containing exclusively BCDDM-generated images, the original RLDs, and a mixed dataset (MXDs) combining both RLDs and FKDs. To maintain evaluation consistency, both FKDs and MXDs utilize the same validation and test sets as RLDs. The respective sizes of these datasets are detailed in Table 2.

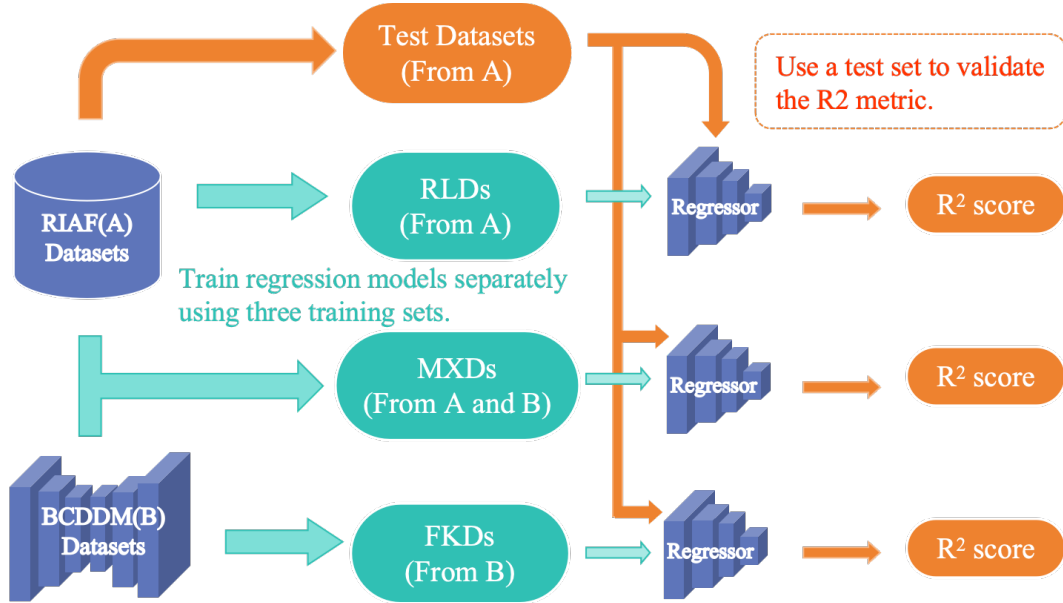


Figure 7. Workflow of Constructing Datasets from Multiple Sources and Evaluating Regression Model Performance. This figure outlines the process of constructing datasets from diverse sources and evaluating the performance of a regression model. It highlights two primary data sources: RIAF Datasets and BCDDM Datasets. The figure underscores the critical step of using a test set to validate the R^2 metric, culminating in the output of the R^2 score to assess the model’s performance.

Table 3. R^2 values for different parameters in three datasets.

Trainset	a	T_e	h_{disk}	M_{BH}	k	PA
RLDs	0.9206	0.9671	0.9841	0.9982	0.9538	0.9012
FKDs	0.7992(↓0.1214)	0.9793(↑0.0122)	0.9683(↓0.0158)	0.9913(↓0.0069)	0.9157(↓0.0381)	0.7789(↓0.1223)
MXDs	0.9645(↑0.0439)	0.9960(↑0.0289)	0.9893(↑0.0052)	0.9982(−0.0000)	0.9762 (↑0.0224)	0.9602(↑0.0590)

As illustrated in Figure 7, we evaluate the performance of three ResNet50 based regressors (He et al. 2016) using different training sets. We employ R^2 as a quantitative measure to assess improvements in parameter estimation accuracy. The R^2 metric is widely used in regression analysis in machine learning. A value closer to 1 indicates a better fit of the model to the data. Let y_i denote the true parameter value of the i -th sample of the test set, \hat{y}_i represent the model’s predicted value for the i -th sample, \bar{y} be the mean parameter value across the test set, and n denote the total number of test samples. The R^2 score is calculated as

$$R^2 = 1 - \frac{\sum_{i=1}^n (y_i - \hat{y}_i)^2}{\sum_{i=1}^n (y_i - \bar{y})^2}. \quad (13)$$

The Table 3 shows the R^2 scores of three datasets experiments. We observe that although the FKDs composed of synthesized images scored lower than RLDs, the model trained on reconstructed images is acceptable for predicting RIAF black hole images. The more important point is that the R^2 scores of MXDs are substantially higher for each parameter compared to those of RLDs. This suggests that incorporating synthetic images exposes the model to a broader spectrum of feature combinations during training, thereby enhancing both the diversity and volume of training data. Consequently, this approach effectively mitigates the risk

Table 4. R^2 values of blurred datasets

Trainset	a	T_e	h_{disk}	M_{BH}	k	PA
RLDs($10\mu as$)	0.9263	0.9756	0.9717	0.9950	0.9751	0.8981
MXDs($10\mu as$)	0.9509 \uparrow	0.9901 \uparrow	0.9737 \uparrow	0.9962 \uparrow	0.9774 \uparrow	0.8070 \downarrow
RLDs($20\mu as$)	0.6893	0.9021	-0.0683	0.9585	0.9598	0.8417
MXDs($20\mu as$)	0.7732 \uparrow	0.9799 \uparrow	-0.3325 \downarrow	0.9865 \uparrow	0.9648 \uparrow	0.8726 \uparrow

289 of model overfitting. Meanwhile, the increase in R^2 value also proves in reverse that BCDDM can learn the
 290 mapping relationship between black hole images and black hole parameters. The synthesized images generated
 291 by BCDDM not only visually resemble real images, but also have a high degree of consistency in statistical
 292 properties and physical meaning. This result demonstrates the feasibility of BCDDM in synthesizing black
 293 hole images. By generating high-quality synthetic images, BCDDM provides a new data augmentation method
 294 for black hole research, which helps overcome the problem of data scarcity and promotes the development of
 295 astrophysics.

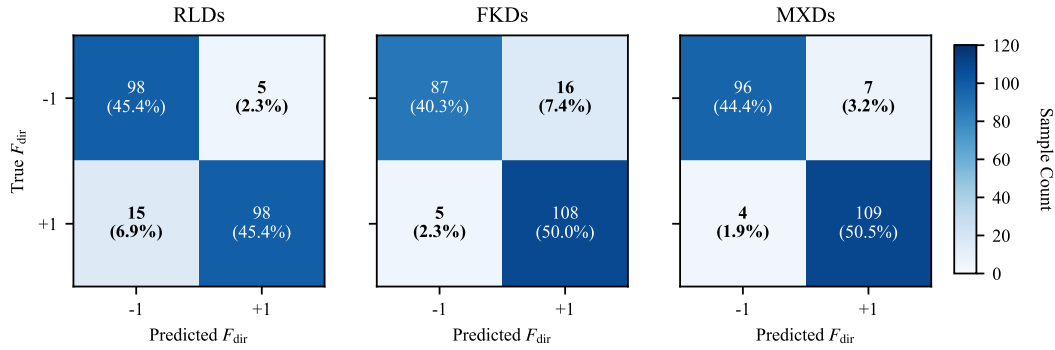


Figure 8. The binary confusion matrix of F_{dir} . The datasets corresponding to the three images are RLDs (left), FKDs (middle), and MXDs (right). The classification accuracies of three training sets for fluid-direction are 92.19%, 89.58% and 94.27%.

296 At the same time, as shown in Figure 8, the confusion matrix for binary classification of fluid-direction also
 297 indicates that MXDs has the best classification performance. This indicates that our method can perform
 298 data augmentation on small-scale datasets, increasing the size of the training dataset and helping the regressor
 299 to more accurately understand the mapping relationship between black hole parameters and images.

300 In addition, in Figure 9, we show the fitting results of the test set samples for RLDs and MXDs. We sorted
 301 the label points by numerical value from small to large and plotted the regressor’s predictions and errors for
 302 the samples. We can clearly see that compared to RLDs, the predicted results of MXDs are closer to the true
 303 values.

304 Due to the limited resolution of actual observations, we evaluated the robustness of black hole parameter
 305 predictions by blurring the images. As shown in Table 4, we blurred the images using Gaussian kernels with

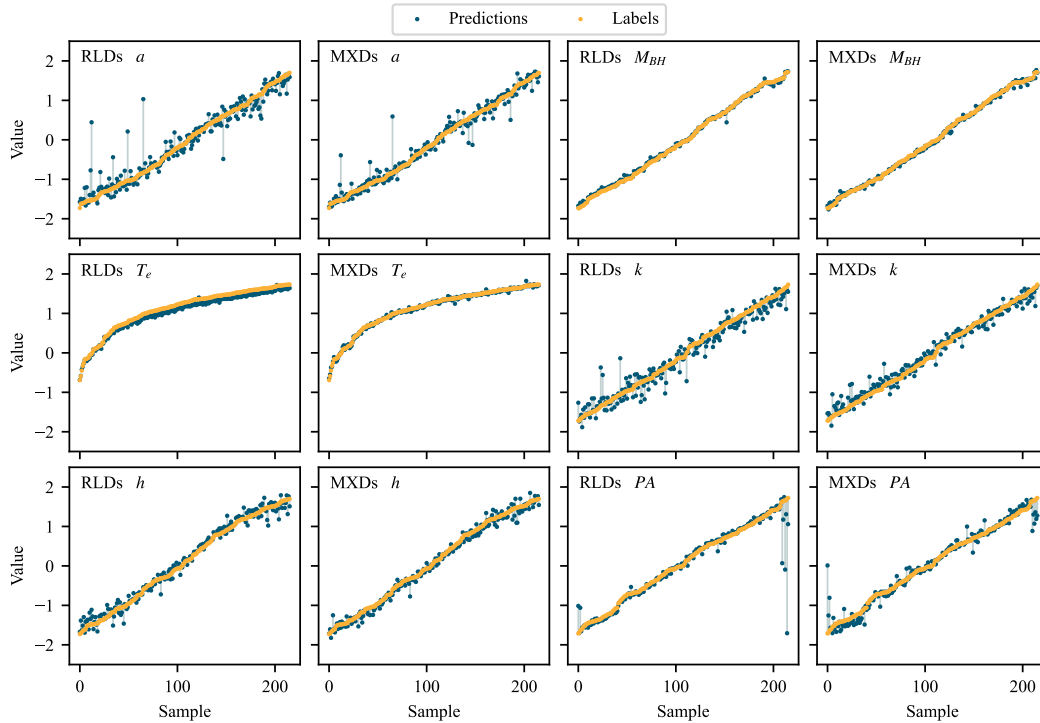


Figure 9. The fitting results of RLDs and MXDs on the test set samples. The prediction error of the test set after training with RLDs for 5000 epochs (left) and the prediction error of the test set after training with MXDs for 5000 epochs (right).

306 FWHM of $10\mu\text{as}$ and $20\mu\text{as}$, respectively. The experimental results quantitatively reveal three phenomena:
 307 when blurring to $10\mu\text{as}$, the regressor maintains high accuracy in predicting each parameter, indicating that
 308 there is no significant loss of various features of the black hole at this scale. At the present EHT resolution of
 309 $20\mu\text{as}$, the prediction accuracy of the accretion disk height h_{disk} drops sharply, and the R^2 of RLDs decreases
 310 from 0.9717 (at $10\mu\text{as}$) to -0.0683, demonstrating the degradation of accretion disk thickness features. In
 311 Figure 10, we present the regression results of blurred datasets. Overall, MXDs show clear advantages over
 312 RLDs. We have ample reason to believe that our proposed method can accurately generate clear black hole
 313 images while preserving the characteristics of black hole parameters. This achievement is expected to provide
 314 strong support and assistance for other data-driven algorithms.

315 4. CONCLUSION

316 In this study, we propose an innovative black hole image generation method named Branch Correction De-
 317 noising Diffusion Model, aimed at effectively enhancing limited scale black hole image data sets and accelerate
 318 the generation of black hole images. By innovatively improving the architecture of the classical diffusion
 319 model, we introduce a parameter correction branch and use a mixed loss function to ensure that the model
 320 can learn both image distribution and black hole parameters simultaneously. The experimental results show

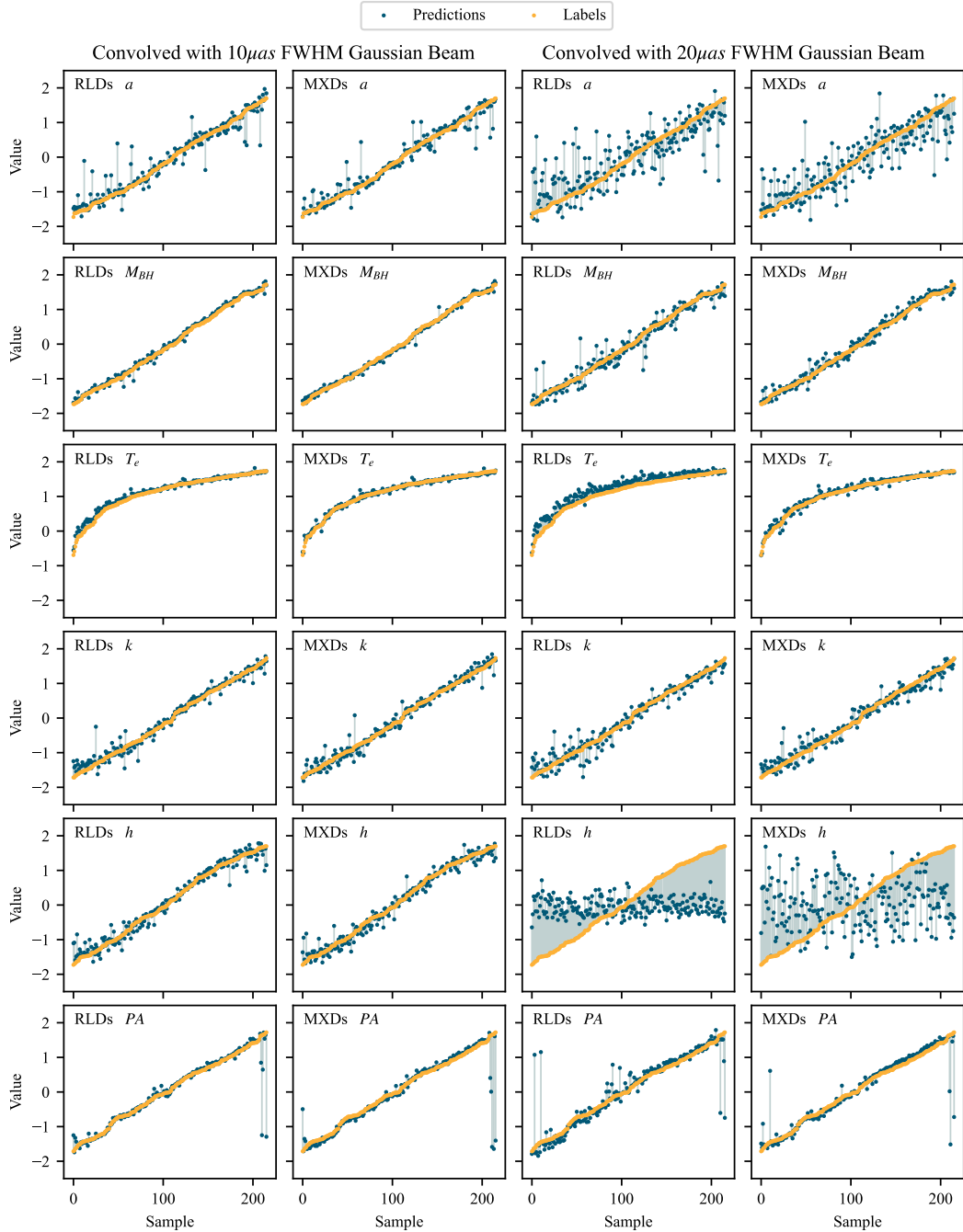


Figure 10. The fitting results of RLDs and MXDs on the test set samples. The prediction error of the test set after training with RLDs for 5000 epochs (left) and the prediction error of the test set after training with MXDs for 5000 epochs (right).

321 that BCDDM can not only generate clear and high-quality black hole images from noisy images, but also
 322 ensure that the features of the generated images correspond accurately to the initial parameters. We used
 323 NRMSE and SSIM to quantify the similarity between GRRT images and BCDDM-generated images with the
 324 same physical parameters and found that all reconstructed images reveal high SSIM values. However, the

325 spatial alignment between BCDDM-generated and GRRT images occasionally varies, resulting in some images
 326 having high NRMSE, which is likely due to the influence of the initial noise distribution during sampling from
 327 pure Gaussian noise. In addition, the model has limited ability to reconstruct images beyond the parameter
 328 range of the original dataset, indicating that the current model mainly focuses on the parameter space it has
 329 been trained on. However, this limitation can be mitigated by expanding the parameter range of the training
 330 dataset.

331 In addition, our research also indicates that the dataset generated by BCDDM is highly consistent with
 332 the training set in terms of statistical properties and physical significance. By mixing generated data with
 333 real data for training a regressor, we found that its performance was significantly better than a regressor
 334 trained solely on real data. This improvement is attributed to the significant increase in the number and
 335 diversity of the training set generated by the data, thereby improving the model's generalization ability. In
 336 the experiment, we used a single RTX 3090 GPU to generate images with a specific radiative flux, achieving an
 337 efficient performance with a generation time of just 5.25 seconds per image. Although the simulated dataset
 338 used in this study is derived from the RIAF model, the BCDDM method is broadly applicable and can be
 339 extended to data from other accretion disk model, with future applications anticipated for a wider range of
 340 accretion disk models. In addition, the polarization information in the black hole image can provide more
 341 information for analyzing the properties of the accretion flow around the black hole ([Event Horizon Telescope
 342 Collaboration et al. 2021a,b, 2024c,b](#)). The images input into our model are single-channel and do not consider
 343 the polarization information of the images. However, encoding the polarization information into multi-channel
 344 images and using neural networks such as the Denoising Diffusion Model to generate polarization images can
 345 be further explored in future work.

346 ACKNOWLEDGMENTS

347 This work was supported by the National Natural Science Foundation of China under Grants No.
 348 12374408, 12475051, 12275078, 12035005; the Natural Science Foundation of Hunan Province under grant No.
 349 2023JJ30384; the science and technology innovation Program of Hunan Province under grant No. 2024RC1050;
 350 and the innovative research group of Hunan Province under Grant No. 2024JJ1006. The authors thank the
 351 anonymous referee for their helpful suggestions regarding the manuscript.

REFERENCES

- 352 Asgar, S., Sahil, A. A., & Nazim Uddin, M. 2023, in
 353 2023 26th International Conference on Computer
 354 and Information Technology (ICIT), 1–5,
 355 doi: [10.1109/ICIT60459.2023.10441276](https://doi.org/10.1109/ICIT60459.2023.10441276)
- 356 Bardeen, J. M. 1973, in *Black Holes (Les Astres
 357 Occlus)*, ed. C. Dewitt & B. S. Dewitt, 215–239

- 358 Broderick, A. E., Fish, V. L., Doleman, S. S., & Loeb,
359 A. 2011a, *ApJ*, 735, 110,
360 doi: [10.1088/0004-637X/735/2/110](https://doi.org/10.1088/0004-637X/735/2/110)
- 361 —. 2011b, *ApJ*, 738, 38,
362 doi: [10.1088/0004-637X/738/1/38](https://doi.org/10.1088/0004-637X/738/1/38)
- 363 Broderick, A. E., Gold, R., Karami, M.,
364 Preciado-López, J. A., et al. 2020, *ApJ*, 897, 139,
365 doi: [10.3847/1538-4357/ab91a4](https://doi.org/10.3847/1538-4357/ab91a4)
- 366 Broderick, A. E., Fish, V. L., Johnson, M. D., et al.
367 2016, *ApJ*, 820, 137,
368 doi: [10.3847/0004-637X/820/2/137](https://doi.org/10.3847/0004-637X/820/2/137)
- 369 Chael, A., Johnson, M. D., & Lupsasca, A. 2021, *ApJ*,
370 918, 6, doi: [10.3847/1538-4357/ac09ee](https://doi.org/10.3847/1538-4357/ac09ee)
- 371 Chan, C.-k., Medeiros, L., Özel, F., & Psaltis, D. 2018,
372 *ApJ*, 867, 59, doi: [10.3847/1538-4357/aadfe5](https://doi.org/10.3847/1538-4357/aadfe5)
- 373 Chang, D., Tiede, P., Johnson, M., & Palumbo, D.
374 2024, in *IAU General Assembly*, 1132,
375 doi: [10.48550/arXiv.2405.04749](https://doi.org/10.48550/arXiv.2405.04749)
- 376 Chen, S., Jing, J., Qian, W.-L., & Wang, B. 2023,
377 *Science China Physics, Mechanics, and Astronomy*,
378 66, 260401, doi: [10.1007/s11433-022-2059-5](https://doi.org/10.1007/s11433-022-2059-5)
- 379 Event Horizon Telescope Collaboration, Akiyama, K.,
380 Alberdi, A., Alef, W., et al. 2019a, *ApJL*, 875, L1,
381 doi: [10.3847/2041-8213/ab0ec7](https://doi.org/10.3847/2041-8213/ab0ec7)
- 382 —. 2019b, *ApJL*, 875, L5,
383 doi: [10.3847/2041-8213/ab0f43](https://doi.org/10.3847/2041-8213/ab0f43)
- 384 —. 2022a, *ApJL*, 930, L12,
385 doi: [10.3847/2041-8213/ac6674](https://doi.org/10.3847/2041-8213/ac6674)
- 386 —. 2022b, *ApJL*, 930, L17,
387 doi: [10.3847/2041-8213/ac6756](https://doi.org/10.3847/2041-8213/ac6756)
- 388 —. 2022c, *ApJL*, 930, L16,
389 doi: [10.3847/2041-8213/ac6672](https://doi.org/10.3847/2041-8213/ac6672)
- 390 —. 2024a, *A&A*, 681, A79,
391 doi: [10.1051/0004-6361/202347932](https://doi.org/10.1051/0004-6361/202347932)
- 392 Event Horizon Telescope Collaboration, Akiyama, K.,
393 Algaba, J. C., et al. 2021a, *ApJL*, 910, L12,
394 doi: [10.3847/2041-8213/abe71d](https://doi.org/10.3847/2041-8213/abe71d)
- 395 —. 2021b, *ApJL*, 910, L13,
396 doi: [10.3847/2041-8213/abe4de](https://doi.org/10.3847/2041-8213/abe4de)
- 397 Event Horizon Telescope Collaboration, Akiyama, K.,
398 Alberdi, A., et al. 2024b, *ApJL*, 964, L26,
399 doi: [10.3847/2041-8213/ad2df1](https://doi.org/10.3847/2041-8213/ad2df1)
- 400 —. 2024c, *ApJL*, 964, L25,
401 doi: [10.3847/2041-8213/ad2df0](https://doi.org/10.3847/2041-8213/ad2df0)
- 402 Falcke, H., Melia, F., & Agol, E. 2000, *ApJL*, 528, L13,
403 doi: [10.1086/312423](https://doi.org/10.1086/312423)
- 404 Fei, N., Gao, Y., Lu, Z., & Xiang, T. 2021, in 2021
405 *IEEE/CVF International Conference on Computer*
406 *Vision (ICCV)*, 142–151
- 407 Gelles, Z., Prather, B. S., Palumbo, D. C. M., Johnson,
408 M. D., et al. 2021, *ApJ*, 912, 39,
409 doi: [10.3847/1538-4357/abee13](https://doi.org/10.3847/1538-4357/abee13)
- 410 Goodfellow, I. J., Pouget-Abadie, J., Mirza, M., Xu,
411 B., et al. 2014, in *Proceedings of the 28th*
412 *International Conference on Neural Information*
413 *Processing Systems - Volume 2, NIPS'14*
414 (Cambridge, MA, USA: MIT Press), 2672–2680
- 415 Gralla, S. E., Holz, D. E., & Wald, R. M. 2019,
416 *PhRvD*, 100, 024018,
417 doi: [10.1103/PhysRevD.100.024018](https://doi.org/10.1103/PhysRevD.100.024018)
- 418 He, K., Zhang, X., Ren, S., & Sun, J. 2016, in 2016
419 *IEEE Conference on Computer Vision and Pattern*
420 *Recognition (CVPR)*, 770–778
- 421 Ho, J., Jain, A., & Abbeel, P. 2020, *Denosing*
422 *Diffusion Probabilistic Models*
- 423 Hochreiter, S., & Schmidhuber, J. 1997, *Neural*
424 *computation*, 9, 1735,
425 doi: [10.1162/neco.1997.9.8.1735](https://doi.org/10.1162/neco.1997.9.8.1735)
- 426 Hou, Y., Huang, J., Mizuno, Y., Guo, M., et al. 2024,
427 *arXiv e-prints*, arXiv:2409.07248,
428 doi: [10.48550/arXiv.2409.07248](https://doi.org/10.48550/arXiv.2409.07248)
- 429 Huang, J., Zheng, L., Guo, M., & Chen, B. 2024,
430 *JCAP*, 2024, 054,
431 doi: [10.1088/1475-7516/2024/11/054](https://doi.org/10.1088/1475-7516/2024/11/054)
- 432 Igmenshchev, I. V., Narayan, R., & Abramowicz,
433 M. A. 2003, *ApJ*, 592, 1042, doi: [10.1086/375769](https://doi.org/10.1086/375769)
- 434 Johnson, M. D., Lupsasca, A., Strominger, A., Wong,
435 G. N., et al. 2020, *Science Advances*, 6, eaaz1310,
436 doi: [10.1126/sciadv.aaz1310](https://doi.org/10.1126/sciadv.aaz1310)
- 437 Kingma, D. P., & Welling, M. 2022, *Auto-Encoding*
438 *Variational Bayes*. <https://arxiv.org/abs/1312.6114>
- 439 Krizhevsky, A., Sutskever, I., & Hinton, G. E. 2012,
440 *Communications of the ACM*, 60, 84
- 441 Liu, X., Chen, S., & Jing, J. 2022, *Science China*
442 *Physics, Mechanics, and Astronomy*, 65, 120411,
443 doi: [10.1007/s11433-022-1946-2](https://doi.org/10.1007/s11433-022-1946-2)
- 444 Luminet, J. P. 1979, *A&A*, 75, 228
- 445 Medeiros, L., Lauer, T. R., Psaltis, D., & Özel, F.
446 2018, *ApJ*, 864, 7, doi: [10.3847/1538-4357/aad37a](https://doi.org/10.3847/1538-4357/aad37a)
- 447 Medeiros, L., Psaltis, D., Lauer, T. R., & Özel, F.
448 2023, *ApJL*, 947, L7, doi: [10.3847/2041-8213/acc32d](https://doi.org/10.3847/2041-8213/acc32d)
- 449 Mizuno, Y., Younsi, Z., Fromm, C. M., Porth, O.,
450 et al. 2018, *Nature Astronomy*, 2, 585,
451 doi: [10.1038/s41550-018-0449-5](https://doi.org/10.1038/s41550-018-0449-5)
- 452 Mohan, A., Protopapas, P., Kunnumkai, K., Garraffo,
453 C., et al. 2024, *MNRAS*, 527, 10965,
454 doi: [10.1093/mnras/stad3797](https://doi.org/10.1093/mnras/stad3797)
- 455 Mościbrodzka, M., & Gammie, C. F. 2018, *MNRAS*,
456 475, 43, doi: [10.1093/mnras/stx3162](https://doi.org/10.1093/mnras/stx3162)
- 457 Moscibrodzka, M. A., & Yfantis, A. I. 2023, *ApJS*, 265,
458 22, doi: [10.3847/1538-4365/acb6f9](https://doi.org/10.3847/1538-4365/acb6f9)
- 459 Narayan, R., Chael, A., Chatterjee, K., Ricarte, A.,
460 et al. 2022, *MNRAS*, 511, 3795,
461 doi: [10.1093/mnras/stac285](https://doi.org/10.1093/mnras/stac285)

- 462 Narayan, R., Igumenshchev, I. V., & Abramowicz,
463 M. A. 2003, PASJ, 55, L69,
464 doi: [10.1093/pasj/55.6.L69](https://doi.org/10.1093/pasj/55.6.L69)
- 465 Narayan, R., Kato, S., & Honma, F. 1997, ApJ, 476,
466 49, doi: [10.1086/303591](https://doi.org/10.1086/303591)
- 467 Narayan, R., Palumbo, D. C. M., Johnson, M. D.,
468 Gelles, Z., et al. 2021, ApJ, 912, 35,
469 doi: [10.3847/1538-4357/abf117](https://doi.org/10.3847/1538-4357/abf117)
- 470 Peng, J., Guo, M., & Feng, X.-H. 2021, PhRvD, 104,
471 124010, doi: [10.1103/PhysRevD.104.124010](https://doi.org/10.1103/PhysRevD.104.124010)
- 472 Pu, H.-Y., Akiyama, K., & Asada, K. 2016a, ApJ, 831,
473 4, doi: [10.3847/0004-637X/831/1/4](https://doi.org/10.3847/0004-637X/831/1/4)
- 474 Pu, H.-Y., & Broderick, A. E. 2018, ApJ, 863, 148,
475 doi: [10.3847/1538-4357/aad086](https://doi.org/10.3847/1538-4357/aad086)
- 476 Pu, H.-Y., Yun, K., Younsi, Z., & Yoon, S.-J. 2016b,
477 ApJ, 820, 105, doi: [10.3847/0004-637X/820/2/105](https://doi.org/10.3847/0004-637X/820/2/105)
- 478 Qin, X., Chen, S., Zhang, Z., & Jing, J. 2022, ApJ,
479 938, 2, doi: [10.3847/1538-4357/ac8f49](https://doi.org/10.3847/1538-4357/ac8f49)
- 480 Qiu, R., Ricarte, A., Narayan, R., Wong, G. N., et al.
481 2023, MNRAS, 520, 4867,
482 doi: [10.1093/mnras/stad466](https://doi.org/10.1093/mnras/stad466)
- 483 Ran, H., Guizilini, V., & Wang, Y. 2024, in
484 Proceedings of the IEEE/CVF Conference on
485 Computer Vision and Pattern Recognition
- 486 SaraerToosi, A., & Broderick, A. E. 2024, ApJ, 967,
487 140, doi: [10.3847/1538-4357/ad3e76](https://doi.org/10.3847/1538-4357/ad3e76)
- 488 Shi, Y., Xia, W., Wang, G., & Mou, X. 2024, IEEE
489 Transactions on Medical Imaging, 43, 3559,
490 doi: [10.1109/TMI.2024.3418652](https://doi.org/10.1109/TMI.2024.3418652)
- 491 Simonyan, K., & Zisserman, A. 2014, Computer
492 Science
- 493 Stephen, K. D., & Kazemi, A. 2014, Geophysical
494 Prospecting, 62, 1009, doi: [10.1111/1365-2478.12109](https://doi.org/10.1111/1365-2478.12109)
- 495 Tu, S., Dai, Q., Cheng, Z.-Q., et al. 2024, in
496 Proceedings of the IEEE/CVF Conference on
497 Computer Vision and Pattern Recognition
- 498 van der Gucht, J., Davelaar, J., Hendriks, L., Porth,
499 O., et al. 2020, A&A, 636, A94,
500 doi: [10.1051/0004-6361/201937014](https://doi.org/10.1051/0004-6361/201937014)
- 501 Vincent, F. H., Paumard, T., Gourgoulhon, E., &
502 Perrin, G. 2011, Classical and Quantum Gravity, 28,
503 225011, doi: [10.1088/0264-9381/28/22/225011](https://doi.org/10.1088/0264-9381/28/22/225011)
- 504 Wan, A., & Ohtani, K. 2000, Journal of Statistical
505 Planning and Inference, 86, 157
- 506 Wang, M., Chen, S., & Jing, J. 2022, Communications
507 in Theoretical Physics, 74, 097401,
508 doi: [10.1088/1572-9494/ac6e5c](https://doi.org/10.1088/1572-9494/ac6e5c)
- 509 Wang, Z., Bovik, A., Sheikh, H., & Simoncelli, E. 2004,
510 IEEE Transactions on Image Processing, 13, 600,
511 doi: [10.1109/TIP.2003.819861](https://doi.org/10.1109/TIP.2003.819861)
- 512 Wang, Z., & Bovik, A. C. 2009, IEEE Signal Processing
513 Magazine, 26, 98, doi: [10.1109/MSP.2008.930649](https://doi.org/10.1109/MSP.2008.930649)
- 514 White, C. J. 2022, ApJS, 262, 28,
515 doi: [10.3847/1538-4365/ac77ef](https://doi.org/10.3847/1538-4365/ac77ef)
- 516 Yfantis, A. I., Zhao, S., Gold, R., Mościbrodzka, M.,
517 et al. 2024, MNRAS, 535, 3181,
518 doi: [10.1093/mnras/stae2509](https://doi.org/10.1093/mnras/stae2509)
- 519 Yuan, F., & Narayan, R. 2014, ARA&A, 52, 529,
520 doi: [10.1146/annurev-astro-082812-141003](https://doi.org/10.1146/annurev-astro-082812-141003)
- 521 Yuan, F., Quataert, E., & Narayan, R. 2003, ApJ, 598,
522 301, doi: [10.1086/378716](https://doi.org/10.1086/378716)
- 523 Zhang, Z., Chen, S., & Jing, J. 2022, European
524 Physical Journal C, 82, 835,
525 doi: [10.1140/epjc/s10052-022-10794-z](https://doi.org/10.1140/epjc/s10052-022-10794-z)
- 526 —. 2024, JCAP, 2024, 027,
527 doi: [10.1088/1475-7516/2024/09/027](https://doi.org/10.1088/1475-7516/2024/09/027)
- 528 Zhang, Z., Hou, Y., Guo, M., & Chen, B. 2024, JCAP,
529 05, 032, doi: [10.1088/1475-7516/2024/05/032](https://doi.org/10.1088/1475-7516/2024/05/032)
- 530 Zheng, Y., Liang, R., ZHENG, K., et al. 2025, in The
531 Thirteenth International Conference on Learning
532 Representations.
533 <https://openreview.net/forum?id=wM2sfVgMDH>